Full length article

# Human osteoblasts grow transitional Si/N apatite in quickly osteointegrated $Si_3N_4$ cervical insert

Giuseppe Pezzotti [a,b,c,d,*], Naoki Oba [a], Wenliang Zhu [e], Elia Marin [a], Alfredo Rondinella [a], Francesco Boschetto [a], Bryan McEntire [f], Kengo Yamamoto [b], B. Sonny Bal [f,g]

[a] Ceramic Physics Laboratory, Kyoto Institute of Technology, Sakyo-ku, Matsugasaki, 606-8126 Kyoto, Japan
[b] Department of Orthopedic Surgery, Tokyo Medical University, 6-7-1 Nishishinjuku, Shinjuku-ku, Tokyo 160-0023, Japan
[c] Department of Molecular Cell Physiology, Graduate School of Medical Science, Kyoto Prefectural University of Medicine, Kamigyo-ku, Kyoto 602-8566, Japan
[d] The Center for Advanced Medical Engineering and Informatics, Osaka University, Yamadaoka, Suita 565-0871 Osaka, Japan
[e] Department of Medical Engineering for Treatment of Bone and Joint Disorders, Osaka University, 2-2 Yamadaoka, Suita, Osaka 565-0854, Japan
[f] Amedica Corporation, 1885 West 2100 South, Salt Lake City, UT 84119, United States
[g] Department of Orthopaedic Surgery, University of Missouri, Columbia, MO 65212, United States

## ARTICLE INFO

## ABSTRACT

Silicon nitride ($Si_3N_4$) ceramics possesses surface chemistry that accelerates bone repair, as previously established by in vitro experiments using both osteosarcoma and mesenchymal cells. The release of silicic acid and nitrogen compounds from the surface $Si_3N_4$ enhanced in vitro cellular activity. The results of this study demonstrate for the first time that the osseointegration behavior previously observed is operative with a peculiar chemistry within the human milieu. Si and N elements stimulated progenitor cell differentiation and osteoblastic activity, which ultimately resulted in accelerated bone ingrowth. At the molecular scale, insight into the effect of silicon and nitrogen ions released from the $Si_3N_4$ surface was obtained through combined histomorphometric analyses, Raman, Fourier-transform-infrared, and X-ray photoelectron spectroscopies. Identical analyses conducted on a polyetheretherketone (PEEK) spinal explant showed no chemical changes and a lower propensity for osteogenic activity. Silicon and nitrogen are key elements in stimulating cells to generate bony apatite with crystallographic imperfections, leading to enhanced bioactivity of $Si_3N_4$ biomedical devices.

### Statement of Significance

This research studies osseointegration processes comparing results from explanted PEEK and $Si_3N_4$ spinal spacers. Data show that the formation of hydroxyapatite on silicon nitride bio-ceramic surfaces happens with a peculiar mechanism inside the human body. Silicon and nitrogen were incorporated inside the bony tissue structure allowing the developing of off-stoichiometric bony apatite and stimulating progenitor cell differentiation/osteoblastic activity. Silicon and nitrogen ions released from the $Si_3N_4$ surface were detected through combined histologic analyses, Raman microspectroscopy, Fourier-transform-infrared, and X-ray photoelectron spectroscopies.

## 1. Introduction

Calcium off-stoichiometry in the hydroxyapatite structure of bone and the wide range of ion substitutes in its crystal structure play fundamental roles in cell differentiation and bone regeneration. Both in vitro and in vivo studies have shown that substitution of aliovalent $(SiO_4)^{4-}$ for $(PO_4)^{3-}$ tetrahedra in synthetic hydroxyapatite accelerates bone formation [1,2]. In effect, off-stoichiometry serves as a barometer for bone remodeling efficiency [3,4]. However, while it is established that electrical charges associated with defectively aliovalent sites on hydroxyapatite promote protein adsorption and osteoblastic activity in vitro [5,6], enhancing osteoinductivity in vivo by Si incorporation into apatite remains an objective of basic research. Note, however, that this "chemical" factor is not the only parameter to be taken into account when designing a load bearing implant in contact with bone. Besides

* Corresponding author at: Ceramic Physics Laboratory, Kyoto Institute of Technology, Sakyo-ku, Matsugasaki, 606-8126 Kyoto, Japan.
E-mail address: pezzotti@kit.ac.jp (G. Pezzotti).

the capacity of achieving an osteogenetic stimulus through surface chemistry, the implant material should also possess a reliably high strength and a Young's modulus compatible with bone in order to avoid bone atrophy and subsequent strength degeneration, a phenomenon so far referred to as bone shielding [7]. Both $Si_3N_4$ and PEEK implants clear up strength reliability issues, and no cases of bone atrophy have so far been clearly identified upon using those biomaterials in spinal implants. Moreover, a recent clinical paper [8], which described a double-blind multi-center randomized controlled trial of silicon nitride versus PEEK cages, has clarified how the former bioceramic material experiences better biocompatible and osteoconductive behaviors as compared to the latter polymer. This has been interpreted as a path to lower complication rates and better fusion through reducing subsidence and migration of the cage.

Previous studies using human osteosarcoma (SaOS-2) and murine mesenchymal (KUSA-A1) cells *in vitro* demonstrated that $Si_3N_4$ possessed an intriguing chemistry capable of increased biogenic apatite formation on both smooth and rough surfaces [9–12]. From these studies, it was determined that enhanced osteogenesis by $Si_3N_4$ depends on several factors including cell mobility (resulting from off-stoichiometry surface sites and modulated electrical charges) and changes in intracellular signaling (due to ions released by the biomaterial). Time-lapse Raman experiments [12], which monitored the metabolism of SaOS-2 cells in contact with $Si_3N_4$, suggested that the release of orthosilicic acid ($H_4SiO_4$) from the ceramic surface had a positive impact consistent with prior reports for Si-doped synthetic apatites [1,2]. This compound, which is the same dissolution product enhancing the activity of bioglasses, was found to be effective in regulating the expression of osteoblastic markers and cell cycle genes [13,14]. Data collected in recent studies using a number of different analytical techniques clearly showed that $Si_3N_4$ surface reactions were actively involved in providing Si ions for cell metabolism [9–12]. One of the main findings from these *in vitro* experiments was that osteoblast cells actually generated a bony structure, which incorporated $(SiO_4)^{4-}$ tetrahedra from silicic acid as building blocks [12]. The morphogenetic activity of the osteoblasts was monitored through expression of osteoprotegerin (OPG) and bone morphogenetic protein (BMP-2); OPG is a potent inhibitor of osteoclastogenetic activity while simultaneously stimulating osteoblasts to increase bone volume and mineral density [13–15]. Independent spectroscopic analyses provided inconfutable evidence that part of the Si moiety entered the Ca-defective hydroxyapatite lattice of the newly formed bone tissue [12].

Consistent with these prior *in vitro* observations, the central hypothesis of this paper is that $Si_3N_4$ spinal fusion devices not only provide adequate structural support, but also facilitate rapid bone regeneration. This hypothesis was tested by molecular level screening of native bone tissue within a retrieved $Si_3N_4$ spinal implant after ~11 months *in vivo*. The output of this investigation demonstrated that:

(i) $Si_3N_4$ surfaces released $Si^{4+}$ and it was subsequently incorporated into newly formed bone tissue.
(ii) $Si^{4+}$ stimulated osteogenesis and accelerated the osteointegration of the $Si_3N_4$ spinal fusion device.
(iii) This mechanism was unique to $Si_3N_4$. We thus confirmed that there was no interaction upregulating the metabolic activity of osteoblasts for the conventional PEEK explant.

This study builds upon previous observation by other authors that ionic Si up-regulates osteogenic markers for wild type cells [14–17]. It was also inspired by *in vivo* testing showing rapid bone regeneration in rat calvarial models in the presence of ionic Si [18]. Addition of this new evidence is expected to spur further in-depth interest into the intriguing chemistry of human bone growth onto $Si_3N_4$ implants.

## 2. Methods

### 2.1. Explanted $Si_3N_4$ and PEEK spinal spacers

The ceramic implant investigated in this research was made of bulk $Si_3N_4$ bioceramic sintered and then hot-isostatically pressed to achieve full density with concurrent addition of $Al_2O_3$ and $Y_2O_3$ additives. The cervical device (16 × 12 × 8 mm, Amedica Corp., Salt Lake City, UT, USA) was retrieved from the C3-C4 level of a 58 year-old male patient in May of 2013 after ~11 months *in vivo* due to an anatomical change requiring removal of the accompanying metallic cervical plate. At the time of primary surgery, a collagen matrix, mixed with a cryopreserved injectable allograft derived from human placental tissues (BioDfactor™; BioD, Memphis, TN, USA), synthetic apatite, and β-tricalcium phosphate, was used for bone grafting. At the time of its removal, the surgeon found the implant well fused within the segment. For comparison, a lumbar PEEK implant (10 × 26 × 12 mm; Amedica Corp.) was retrieved from a 60 year-old male patient ~14 months after implantation due to non-union.

### 2.2. Sample preparation and histological analyses

Both implants were subjected to careful dehydration, staining, and histomorphometric analyses. Gross photographs of the explanted devices were taken at various angles followed by 3D micro-CT scans and microradiographs (43855A; Faxitron, Wheeling, IL, USA) at 1.5 mA, 70 kVp with an exposure time of 20 s. Appositional Bone Index (ABI) analyses were acquired within the graft hole after dividing the scanned area into different sectors. Measurements were made using an automatic image analysis system (IQ Materials, Media Cybernetics, Inc., Silver Spring, MD, USA). Then, samples were prepared for scanning electron microscopy (SEM) analyses to determine the amount of bone present within the graft hole. Each specimen was fixed in 10% neutral buffered formalin for 72 h, then dehydrated in ascending grades of ethanol over a period of 72 h, infiltrated, and then embedded into methyl methacrylate for a period of 30 days. After the infiltrated monomer was polymerized, 2 ∼ 3 mm thick sections were acquired using a custom, water-cooled, high-speed cut-off saw. Standard metallography techniques were then utilized to grind and polish the specimens to an optical finish. SEM imaging was obtained at 20 kV and ~1.1 nA using a thermal type microscope (JSM-6610, JEOL, Peabody, MA, USA) equipped with a back-scattered electron (BSE) detector and imaging capture software. Following SEM imaging, some sections were ground to a thickness of approximately 75 μm and stained with Sanderson's Rapid Bone Stain™. The stained sections were then visually examined using a light microscope (Nikon E600, Nikon Inc., Melville, NY, USA) equipped with image capturing software (Magnafire SP, Optronics, Goleta, CA, USA).

### 2.3. Molecular spectroscopy analyses

X-ray photoelectron spectroscopy (XPS) was performed using a spectrometer (Axis Ultra, Kratos, Manchester, UK) employing an Al-k$_\alpha$ monochromatic X-ray source. Low-resolution spectral scans were conducted using a pass energy of 160 eV with a compositional resolution of ~0.1 at.%. High resolution scans in spectral interval of interest were conducted using a pass energy of 40 eV, which improved the compositional resolution to approximately 0.01 at.%. The analysis area was set at 700 μm × 300 μm in order

to average out polyphasic compositional heterogeneities at each sample's surface. Data were processed using commercially available software (CasaXPS, Casa Software Ltd., UK). Charging effects were minimized by applying ultrahigh vacuum-rated colloidal silver (Ted Pella, Inc., Redding, CA, USA) to the contact points between the samples and the fixture and by using a low-energy electron source. All reported data were acquired following argon sputtering to remove adsorbed surface contaminants using a beam energy of 4.2 keV, gun angle with respect to sample of 45°, raster area of 3 mm × 3 mm, and a sample current of approximately 2 μA.

Raman spectra were acquired using a confocal (optical) microprobe at room temperature and a single monochromator (T-64000, Jobin-Yvon/Horiba Group, Kyoto, Japan) equipped with a nitrogen-cooled 1024 × 256 pixels CCD camera (CCD-3500V, Horiba Ltd., Kyoto, Japan). Raman data were analyzed by commercially available software (LabSpec, Horiba/Jobin-Yvon, Kyoto, Japan). The excitation frequency used in the experiment was a 532 nm blue line of an Ar-ion laser operating at a power of 100 mW. The spectrum integration time was typically 30 s with the recorded spectra being averaged over three successive measurements. A confocal configuration of the Raman probe was adopted throughout all the experiments. A 100x objective lens was employed in order to exclude the photons scattered from out-of-focus regions, thus obtaining a shallow probe depth of <4 μm. A signal from a He-Ne lamp was employed for all measurements as an internal reference for Raman peak positions. Raman band parameters were obtained by fitting the raw experimental spectra with mixed Lorentzian-Gaussian curves.

Fourier Transform Infrared Spectroscopy (FT-IR) was carried out using the imaging system Spotlight 200 (Perkin Elmer, Waltham, Massachusetts, USA). FT-IR spectra were acquired at aperture size of $200 \times 200\ \mu m^2$.

### 2.4. Statistical methods

Measurements of bone fractional contents values were obtained through measurements on adjacent sectors of the samples. XPS analyses, very sensitive to compositional heterogeneities on the sample's surfaces, were performed on areas 700 μm × 300 μm. In order to average out the influence of heterogeneities on the experimental results, we combined a wide scan area with 10 scan repetitions on each investigated region ($n = 10$). Maps of 9 Raman spectra were collected for each data point with averaging each spectrum over 3 successive scans. FTIR analysis was also performed three times for each location and average spectra presented. Student's t-test was performed to analyze statistical differences between $Si_3N_4$ and PEEK obtaining $p < 0.05$.

## 3. Experimental results

### 3.1. Histological analyses

Fig. 1 shows the $Si_3N_4$ cervical implant from different angular views (cf., labels in the inset and explanations in the caption). These photographs clearly indicate abundant bone residue at both the superior and inferior surfaces of the device. The micro-CT scanning image of Fig. 2(a) demonstrates reasonably uniform bone ingrowth throughout the length of the graft hole (GH). A microradiograph of the explanted device is shown in Fig. 2(b). A series of high-resolution microradiographs were used for analyzing the fraction of bone within the GH during the implant's in vivo service. The analyzed area was arbitrarily divided into three longitudinal sectors, each of which was in turn finely scanned over its entire area (Fig. 2(b)). The bone volume measured by image analysis on microradiographs of each sector are reported in Table 1 for average, median, maximum, minimum, and standard deviation (i.e., with respect to each sub-sector). Upon comparing Fig. 2(b) and Table 1, it clearly appears that sector 3, which was the inferior surface of the implant (i.e., closest to level C4) developed the highest fraction of bone (average and maximum values of 48.72 and 74.47 vol%, respectively). The remaining two sectors were, on average, almost equivalent to each other in terms of bone development, with average bone fractions ~29% lower than that recorded in sector 3. However, sector 1, the superior surface (e.g., closest to level C3), showed a maximum bone fraction significantly higher than sector 2 (62.21 vs. 52.05 vol%). It became clear from the microradiographic analyses that sub-sectors with the most mineralization were located in the mechanically stressed zones as a consequence of load bearing at the implant/vertebrae interfaces. Fig. 2(c) shows a thin section of the $Si_3N_4$ retrieval, which was utilized for molecular spectroscopy analyses as discussed in the next sub-section.

Fig. 3(a) and (b) represent low and high magnification BSE micrographs, respectively. These images demonstrated that bone growth followed the contours of the silicon nitride implant within the GH. The bright white particles in the image of Fig. 3(b) represent synthetic hydroxyapatite from the filler (described in Section 2.1), while the extended grey zones represent the newly formed bone. The manner in which the bone followed the contour of the $Si_3N_4$ implant infers that the bone has conspicuously remodeled to the geometry of the implant with excellent connectivity between the host vertebrae. Morphological details of the bony structure shown in Fig. 3(b) clarify how bone ingrowth remodeled around the filler within the GH.

Light microscopy analyses of stained samples (Fig. 4) showed mature bone formation (pink areas) throughout the entire GH zone
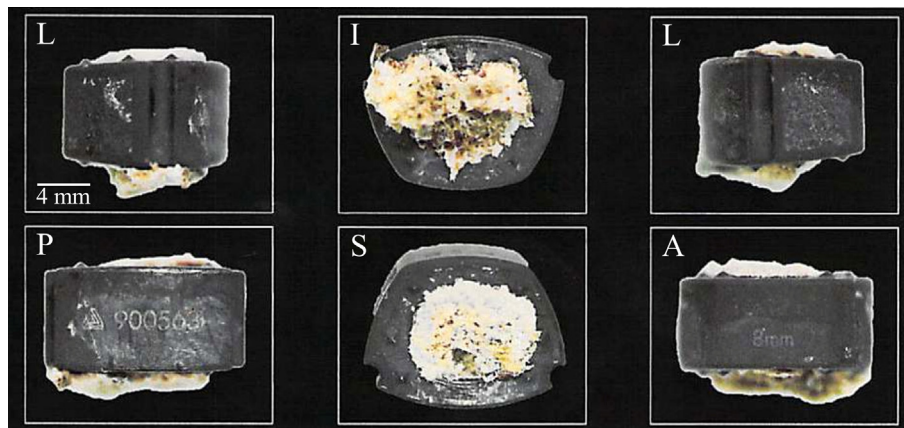


**Fig. 1.** Different views of the $Si_3N_4$ cervical insert after explantation: A = anterior, P = posterior, S = superior, I = inferior, and L = lateral. Note the abundant amount of bone developed above and below the graft hole (GH).
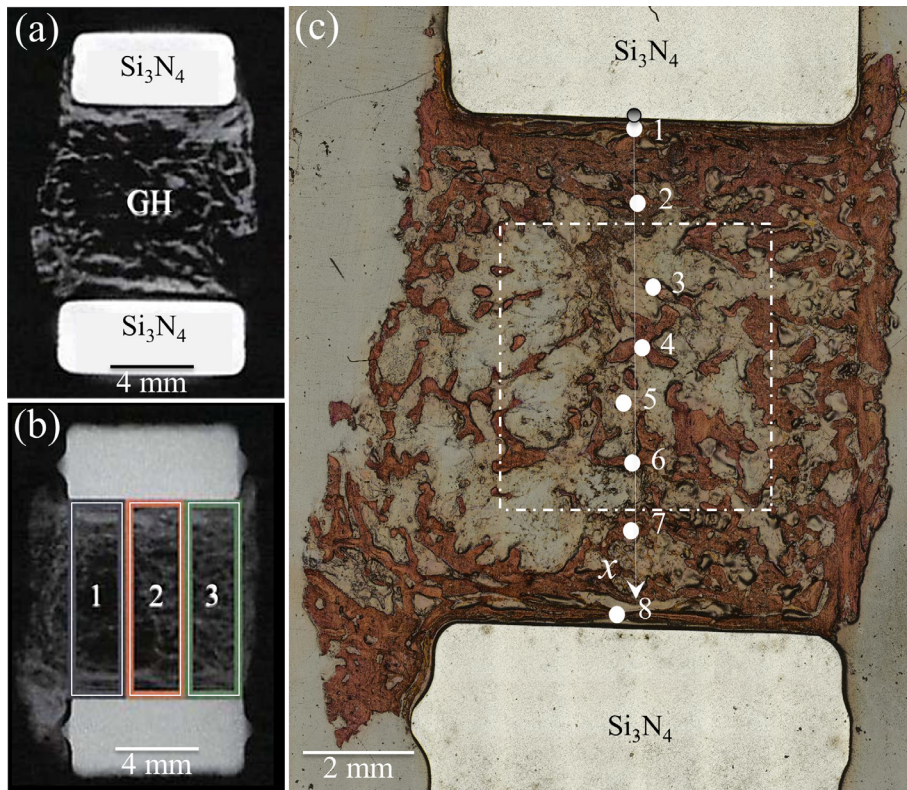
**Fig. 2.** Micro-CT image (a) and microradiograph (b) of the explanted device. In the latter image, the analyzed area was divided into three longitudinal sections. In (c), a thin section is shown of the $Si_3N_4$ retrieval, which was employed for molecular spectroscopy analyses. Eight locations for the Raman profile analyses and the broken square where FT-IR analyses were conducted are also indicated.

**Table 1**

Bone fractional contents measured by image analysis on $Si_3N_4$ implant microradiographs of each sector of Fig. 2(b) are given as average, median, maximum, minimum, and standard deviation values.

| Bone fraction (vol.%) | Sector 1 | Sector 2 | Sector 3 |
|---|---|---|---|
| Average value | 34.34 | 35.16 | 48.72 |
| Standard deviation | 13.70 | 11.09 | 15.79 |
| Median value | 31.58 | 33.78 | 47.90 |
| Maximum value | 62.21 | 52.05 | 74.47 |
| Minimum value | 12.63 | 23.03 | 23.87 |

and even along the outer margin of the $Si_3N_4$ implant (in (a) and (b), respectively). The bone followed the shape of the implant within the GH and around the curved edges, transversing the

inferior to superior surface. It is remarkable that bone formation occurred even on the outer surface of the implant (Fig.4(b)), demonstrating strong osteogenetic stimulus at the $Si_3N_4$'s surface.

ABI analyses from light microscopy images performed on the three sectors inside the GH confirmed the data obtained by image analysis on microradiographs. A fraction of 80.88% fibrous tissue interposition was found with an average of 19.12 ± 11.49% bone contact in the GH. Sector 3 had the highest ABI with 30.89% bone contact, while sectors 2 and 3 displayed fractions of 7.93 and 18.55%, respectively.

A set of histological analyses similar to those shown in Figs. 1–4 for the $Si_3N_4$ retrieval were performed on a conventional PEEK retrieval using the same criteria. The PEEK implant remained in service in its human patient for a period of time slightly longer
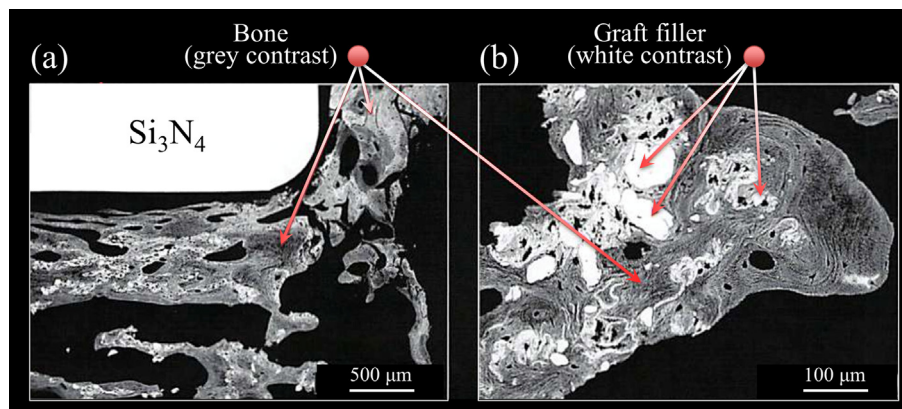


**Fig. 3.** Low (a) and high (b) magnification BSE cross-sectional micrographs of bone ingrowth within the GH; bright white particles are synthetic hydroxyapatite from the filler, while grey zones are the bony apatite.
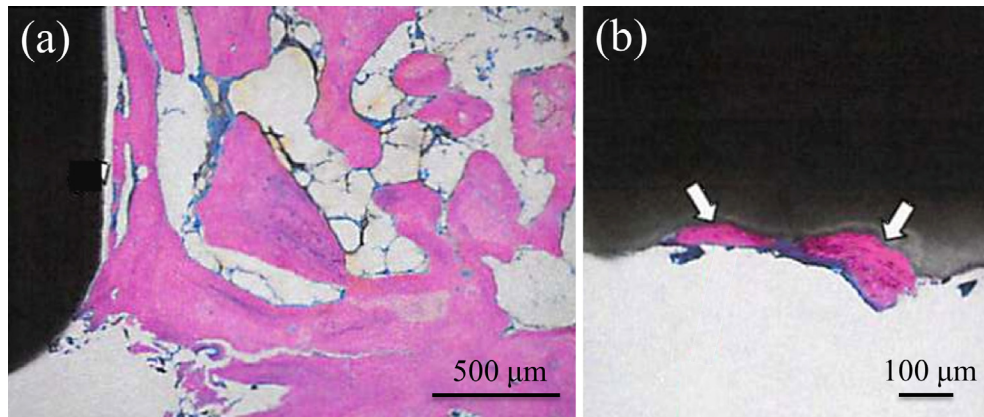
**Fig. 4.** (a) Light microscopy analyses of stained samples showing mature bone formation (pink areas) throughout the GH zone; and, (b) bone enclaves grown along the outer margin of the $Si_3N_4$ implant. (For interpretation of the references to colour in this figure legend, the reader is referred to the web version of this article.)
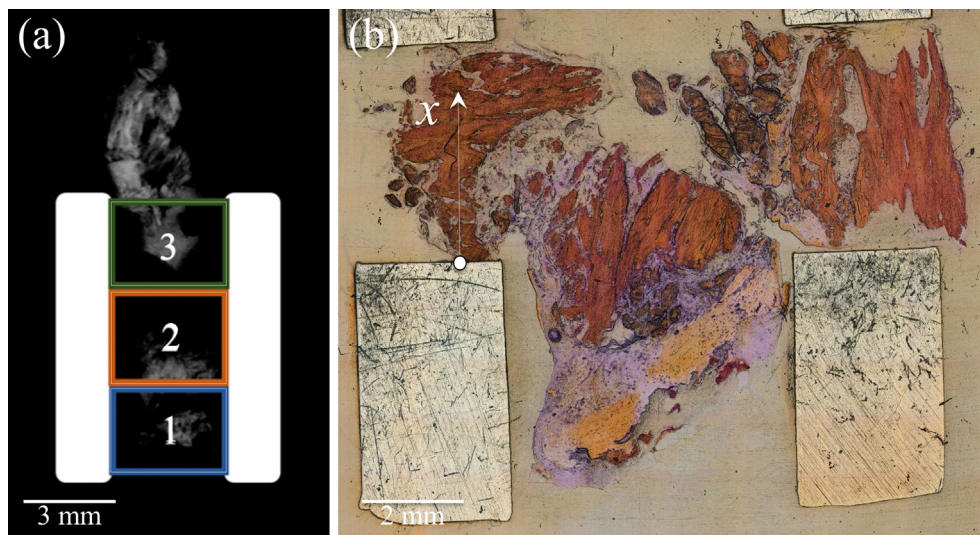


**Fig. 5.** (a) Microradiograph of a retrieved lumbar implant made of PEEK with the GH zone divided into three sectors; and, in (b), a thin section is shown of the PEEK retrieval, which was employed for molecular spectroscopy analyses. The abscissa, $x$, shows spot locations for the Raman profile analyses.

but yet comparable with that of the $Si_3N_4$ implant (*i.e.*, ~14 vs. ~11 mos.). The results of the analyses on the PEEK implant are summarized in Fig. 5. In Fig.5(a), a microradiograph of the implant is shown with the GH zone divided into three sectors. Image analysis data of bone fraction are summarized in Table 2.

A very low amount of bone was found within the three sectors averaging a total of 4.41 ± 9.09%. Clearly, it appears that no chemical stimulus was available from the PEEK implant to enhance bone ingrowth at its surface. Unlike the $Si_3N_4$ implant, which showed a copious amount of bone at the interface between implant and vertebral host bone, the highest amount of bone in the PEEK implant was found in the intermediate sector 2 (average 9.49%). This obser-

**Table 2**
Bone fractional contents measured by image analysis on PEEK implant microradiographs of each sector of Fig. 5(a) are given as average, median, maximum, minimum, and standard deviation values.

| Bone fraction (Vol.%) | Sector 1 | Sector 2 | Sector 3 |
|---|---|---|---|
| Average value | 0.29 | 9.49 | 3.45 |
| Standard deviation | 0.44 | 14.48 | 4.30 |
| Median value | 0.08 | 0.57 | 1.05 |
| Maximum value | 1.12 | 31.83 | 9.57 |
| Minimum value | 0.00 | 0.01 | 0.01 |

vation confirmed that the "soft" contact between PEEK and host bone releases local stresses and gives no stimulus to bone formation. ABI analyses on light micrographs were consistent with image analysis results on microradiographs and showed an average of 0.43 ± 0.75% bone contact and 99.57% fibrous tissue interposition within the graft hole of the 3 sectors analyzed. Bone formation and ABI bone contact in the GH are represented by very low fractions. They also suggest no interaction of the implant with the human body. PEEK only serves a mechanical function as a spacer between vertebrae. Note that the current analysis of bone ingrowth into the PEEK implant is consistent with a goat animal model presented by Sinclair et al. [19] They reported an ABI fraction of 1.27 ± 1.11% for PEEK in their animal study. Fig. 5(b) shows a thin section of the PEEK retrieval, produced in the same way as that shown in Fig. 2(c) for the $Si_3N_4$ implant. This thin section was employed for molecular spectroscopy analyses as discussed in the next sub-section.

### 3.2. Molecular spectroscopy analyses

The strong P-O stretching mode of bony apatite at ~960 cm$^{-1}$ was utilized in the Raman spectroscopic analyses. Fig. 6(a) shows a series of 8 average Raman spectra collected from the $Si_3N_4$ spinal
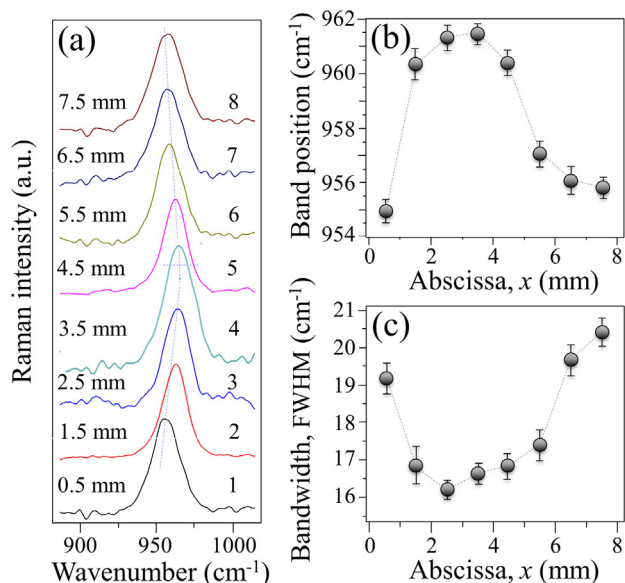
**Fig. 6.** A series of 8 average Raman spectra collected in the $Si_3N_4$ spinal retrieval at locations labeled $1 \sim 8$ along the abscissa, $x$, of Fig. 2(c). In (b) and (c), band position at maximum and FWHM are given with their standard deviations as functions of the abscissa, $x$, respectively.



**Fig. 7.** The P-O stretching Raman band after deconvolution into two sub-bands $A_1$ and $A2$ for the average spectra collected on the $Si_3N_4$ retrieval at locations 1 (a) and 4 (b) as located in Fig. 2(c).

retrieval at the locations labeled $1 \sim 8$ along the abscissa, $x$, in Fig. 2(c). Each average spectrum of the series represents an area of $100 \times 100 \ \mu m^2$ over which maps of 100 spectra per each area were collected. Clear trends were seen both in band position and morphology as a function of distance from the $Si_3N_4$ implant interface. As a first approximation, Raman band morphology was assessed by locating the band's full width at half maximum (FWHM). In Fig. 6(b) and (c) are plotted band position at maximum and bandwidth (FWHM) as functions of the abscissa, $x$, respectively. As seen, the P-O stretching band was significantly shifted toward lower frequencies and its FWHM broadened nearest the interfaces with the $Si_3N_4$ implant; in Fig. 6(b) and (c) are presented maximum and minimum values at the center of the implant, respectively.

Fig. 7 provides details of the P-O stretching Raman band morphology after deconvolution into two sub-bands for the average spectra at locations 1 and 4 (in (a) and (b), respectively). The average bands given in Fig. 7 represented the two limiting cases in terms of band shift and FWHM in the spectroscopic profile depicted in Fig. 6. It can be noted that the frequency shift toward lower frequencies, band broadening, and the associated band asymmetry arose from the presence of a sub-band located at $\sim$950 cm$^{-1}$ (labeled $A_1$ in Fig. 7) in addition to the main component at $\sim$960 cm$^{-1}$ (labeled $A_2$). The physical meaning of the low-frequency sub-band will be discussed in detail in the next section.

Raman data were also acquired on the bony apatite adhering to the external surface of the $Si_3N_4$ implant. The results, provided in Fig. 8, were remarkably similar to the measurements made on the implant's cross-section (cf., Figs. 2 and 6). A Raman line scan along the abscissa, $x$, for the area shown in Fig. 8(a) again revealed a trend of significantly lower frequencies near the $Si_3N_4$ surface and a gradual increase in frequency until a saturated value was reached at a distance of $x \approx 250 \ \mu m$ (Fig. 8(b)). A similar trend was also found for band morphology, expressed here as the areal fraction of the main sub-band $A_1$ over the area of the entire P-O stretching Raman band (Fig. 8(c)). This areal ratio tended to unity with increasing distance (i.e., abscissa, $x$) from the $Si_3N_4$ surface and reached saturation at $x \approx 350 \ \mu m$.
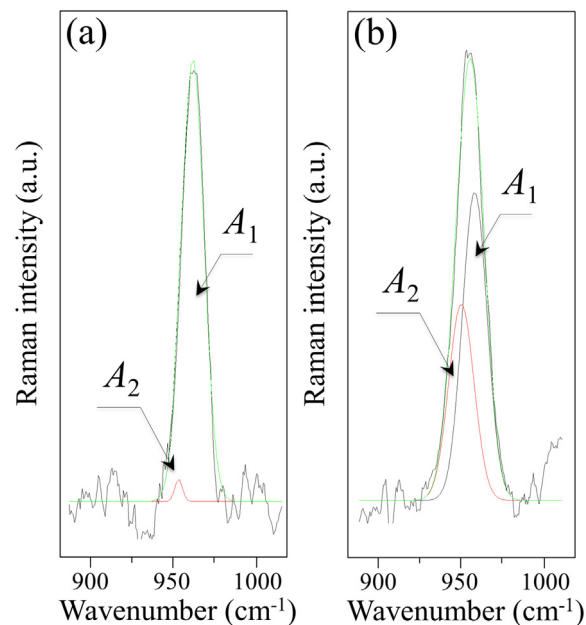
As depicted in Fig. 5(b), the PEEK retrieval was examined using this same Raman scanning and analysis procedure. Results of its characterization are provided in Fig. 9. They show the average P-O stretching band for apatite found near the surface of the PEEK retrieval. However, analyses of band positions and FWHM in Fig. 9(b) and (c), respectively, failed to detect any clear trends as a function of distance from the implant's surface (i.e., abscissa, $x$). In-spite of some scatter in the data, the P-O band's location was conspicuously centered at $\sim$960 cm$^{-1}$ and its FWHM fluctuated within the interval $15 \sim 17.5$ cm$^{-1}$. This result was clearly narrower the data acquired for apatite grown near $Si_3N_4$ surface (i.e., >19 cm$^{-1}$; cf., Fig. 6(c)).

XPS analyses were conducted on the $Si_3N_4$ explant in an effort to clarify the origin of the altered morphology of the P-O stretching band of the native apatite. Fig. 10(a) shows the section of the $Si_3N_4$ implant with bone ingrowth where the XPS analyses were performed (i.e., two separate measurements in Zones A and B). In Fig. 10(b)–(e), the Ca $2p_{1/2}$/Ca $2p_{3/2}$, Si $2p$, N $1s$, and O $1s$ edges of the XPS spectrum are respectively represented as average bands of the two investigated zones. The information obtained from the spectrum shown in Fig. 10(b) was limited because of an inability to distinguish between Ca-O and Ca-N bonds (i.e., there binding energy differed by only minimal amounts). However, the Si $2p$ spectrum of Fig. 10(c) clearly showed the existence of both Si-O and Si-N bonds within the bony apatite, while no free Si and $SiO_2$ (at 99.4 and 103.5 eV, respectively) could be detected. Moreover, the N $1s$ spectrum (Fig. 10(d)) confirmed that elemental nitrogen was actively involved in bonding with Si, C, and Si-O in the bone structure. In addition to the expected O-Ca and P-O-H bonds, the O $1s$ edge (Fig. 10(e)) provided the most straightforward evidence for the existence of O-Si bonds. Table 3 summarizes the XPS data. Computed atomic fractions for each detected bond are listed including the results of C $1s$ edge, whose spectrum was not shown in Fig. 10. According to this XPS analyses, the O-Ca and O-Si fractions were 83.3% and 14.8%, respectively, while N-Si-O bonds represented 10.6% of the in vivo bony apatite structure.

An additional examination of the bony apatite formed inside the $Si_3N_4$ implant was performed by FT-IR spectroscopy. Fig. 11(a)
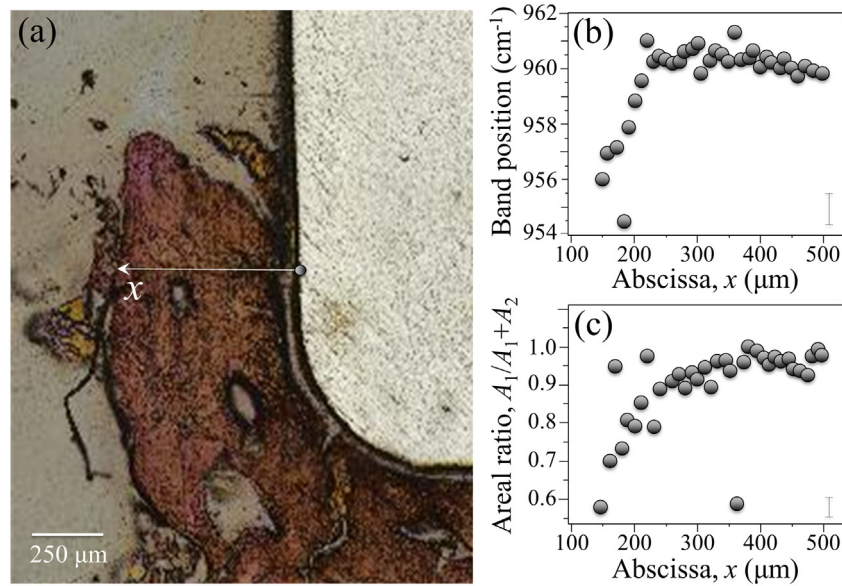
**Fig. 8.** (a) Location at which a Raman line scan was performed along the abscissa, x, on the bony apatite grown on the external surface of the $Si_3N_4$ retrieval; in (b) and (c), trends for frequency shift and of the $A_1$ areal fraction over the total band area, respectively, as functions of the distance, x, from the $Si_3N_4$ surface. Error bars (standard deviations) are shown in inset to (b) and (c).
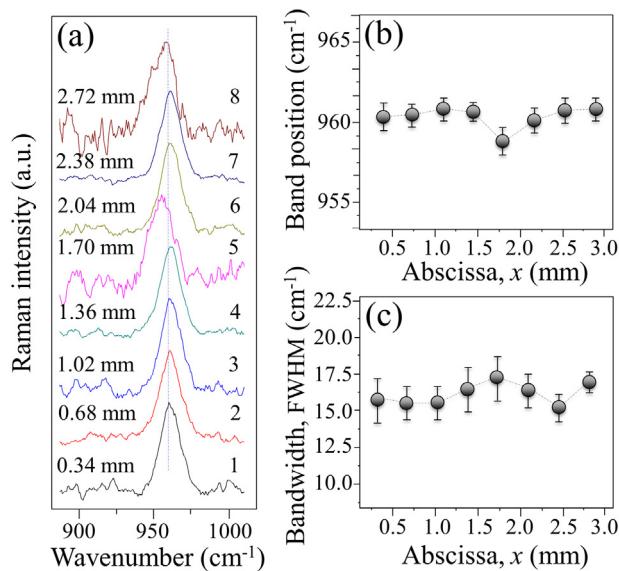


**Fig. 9.** A series of 8 average Raman spectra collected on the PEEK lumbar retrieval along the abscissa, x, in Fig. 5(b). In (b) and (c), band position at maximum and FWHM are given with their standard deviations as functions of the abscissa, x, respectively.

shows the FT-IR spectrum for the central area of the sample in Fig. 2(c), (cf., area within the broken square). This complex and overlapping spectrum was deconvoluted and labeled according to literature data [20–25]. Contributions from protein and collagen bonds appeared in the higher frequency ranges between 1100 and 1300 cm$^{-1}$ (labeled as "organic" in Fig. 11). Strong overlapping bands for tricalcium phosphate (α- and β-TCP), hydroxyapatite $(PO_4)^{3-}$, and organic bonds appeared at low- $(600 \sim 800$ cm$^{-1})$ and intermediate-frequencies $(950 \sim 1100$ cm$^{-1})$ along with $(SiO_4)^{4-}$ tetrahedra (cf., labels in Fig. 11(a)). However, only the weak shoulder at around 750 cm$^{-1}$ did not overlap with other organic or inorganic phases [23]. The zone between 800 and 950 cm$^{-1}$ (shown in Fig. 11(b)) is largely silent for TCP and hydrox-

yapatite phases, except for a weak band at ~878 cm$^{-1}$, which belongs to O-C-O bending in $(CO_3)$ [26]. This vibrational zone provided the clearest fingerprint for the modified chemistry of the bony apatite. It showed a relatively pronounced shoulder at 893 cm$^{-1}$ belonging to the triply degenerate asymmetric stretching of the $(SiO_4)^{4-}$ tetrahedra [23]. An additional band at ~932 cm$^{-1}$ was related to the $(SiO_4)^{4-}$ tetrahedra, but it was overlapped by Si-OH bond vibrations (also present at 840 cm$^{-1}$), while another band at ~873 cm$^{-1}$ was assigned to Si in silica (Si-O-Si) [23].

## 4. Discussion

Three independent spectroscopic probes were used to analyze a cervical intervertebral spinal spacer made from $Si_3N_4$ after being in vivo for only ~11 months. All three methods pointed to the incorporation of $(SiO_4)^{4-}$ tetrahedra within the bony hydroxyapatite structure grown by human osteoblasts. Each method provided a unique chemical fingerprint of the structural modifications within the apatite phase as a function of distance from the $Si_3N_4$ interface. For the Raman analysis, it was the peculiar change in frequency and morphology of the P-O stretching band. The XPS analyses demonstrated the presence of ~15 at. % O-Si bonds were substituted for Ca-O bonds. Finally, the FT-IF spectrum provided a clear shoulder of asymmetric stretching for the $(SiO_4)^{4-}$ tetrahedra at 893 cm$^{-1}$. While these findings confirmed previously published in vitro studies [9–12], the incorporation of nitrogen in addition to silicon within the structure of biogenic hydroxyapatite represented a novel discovery. Elemental nitrogen was found by XPS analyses to be bonded to Ca and Si, suggesting that it substitutionally replaces oxygen in both the $(PO_4)^{3-}$ and $(SiO_4)^{4-}$ tetrahedra, and in OH groups as well. It is noteworthy that the different Raman trends observed for the $Si_3N_4$ and PEEK explants of this study are consistent with fundamental crystallographic data presented by Zou et al. [27] In an attempt to understand the reasons for the enhanced bioactivity of silicon-doped apatites, they examined both pure and silicon substituted synthetic hydroxyapatites by XRD and Raman spectroscopy. They found that silicon was readily incorporated
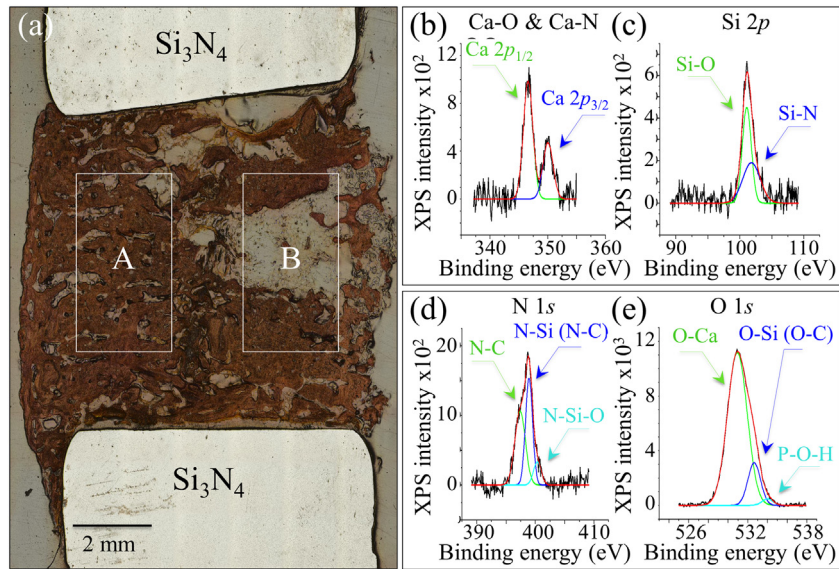
**Fig. 10.** A thin section of the $Si_3N_4$ implant on which XPS analyses were performed in two separate measurements Zones A and B; In (b), (c), (d), and (e), the Ca $2p_{1/2}$/Ca $2p_{3/2}$, Si $2p$, N 1s, and O 1s edges of the XPS spectrum are represented, respectively, as average bands of the two zones A and B. Deconvoluted sub-bands are shown in inset.

**Table 3**
Summary of the XPS data with the computed fractions and related standard deviations for each of the detected atomic bonds.

| Element | Band | Binding Energy (eV) | Assignment | Percentage (%) |
|---|---|---|---|---|
| Si $2p$ | 1 | 101.1 | Si-O | 55.1 ± 1.2 |
| | 2 | 101.8 | Si-N | 44.9 ± 0.9 |
| O 1s | 1 | 530.9 | O-Ca | 83.3 ± 0.8 |
| | 2 | 532.6 | O-Si; O-C | 14.8 ± 1.1 |
| | 3 | 534.0 | P-O-H | 1.9 ± 0.5 |
| N 1s | 1 | 397.4 | N-Ca | 45.3 ± 1.8 |
| | 2 | 398.9 | N-Si; N-C | 44.1 ± 0.7 |
| | 3 | 400.3 | N-Si-O | 10.6 ± 1.1 |
| C 1s | 1 | 283.9 | C-C | 64.4 ± 1.5 |
| | 2 | 285.5 | C-N | 22.8 ± 0.6 |
| | 3 | 287.5 | C-O/C=O | 12.8 ± 0.7 |
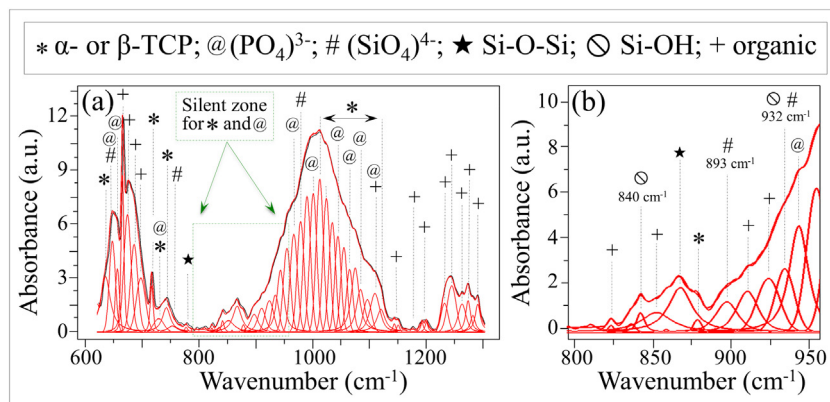


**Fig. 11.** (a) Average deconvoluted FT-IR spectrum retrieved in the broken square area of the sample slice of Fig. 2(c); sub-bands are labeled in inset. In (b), the silent zone for TCP and hydroxyapatite phase at $800 \sim 950$ cm$^{-1}$ is enlarged, which revealed an isolated sub-band at 893 cm$^{-1}$. This band belongs to the triply degenerate asymmetric stretching of the $(SiO_4)^{4-}$ tetrahedra in the hydroxyapatite structure.

into the apatite lattice structure as $(SiO_4)^{4-}$ tetrahedra. The Raman spectroscopic analyses of the $Si_3N_4$ explant from the current study demonstrated that this same chemical fingerprint was present in native hydroxyapatite grown within the human body. Conversely, Raman scans of the native apatite on the PEEK explant failed to detect any substitutional ions or structural changes.

An assembly of $(SiO_4)^{4-}$ tetrahedra and N anions substituting for $(PO_4)^{3-}$ tetrahedra and OH$^-$, respectively, allows for a modified hexagonal apatite symmetry with peculiar characteristics when compared to the conventional bony apatite (Fig. 12(a)). The 4– rather than 3– charge of the tetrahedra requires a different arrangement for O anions and their corresponding vacancies. These two structural modifications are the origin of variations both in the
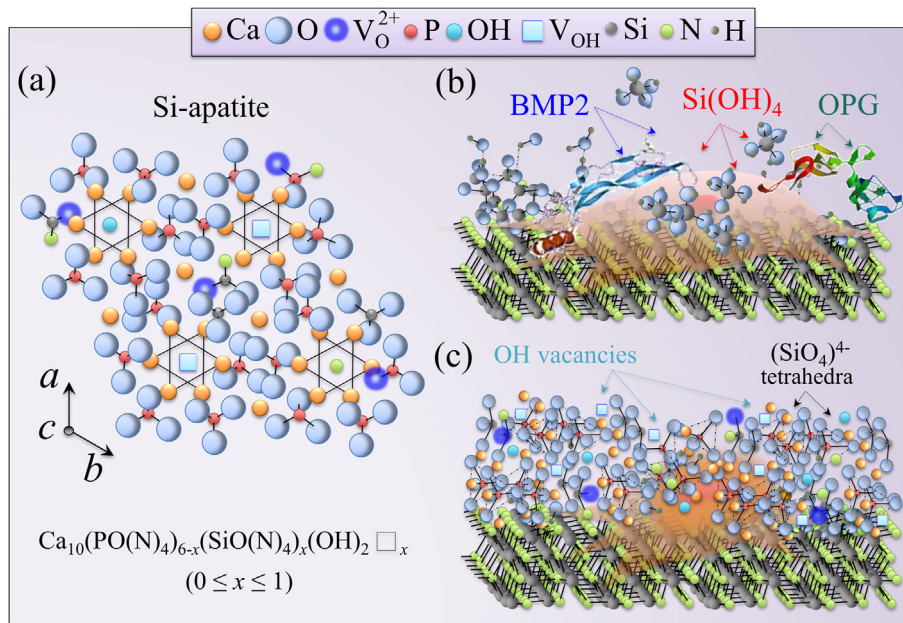
Fig. 12. (a) *c*-axis view of the structure of bony apatite formed in the human body in near the surface of the Si$_3$N$_4$ device. Schematic drawings are shown of the early stage of enhanced signaling of mature osteoblasts on the Si$_3$N$_4$ surface, and, (b) Si-apatite formation with incorporation of N elements substitutional for oxygen in both (PO$_4$)$^{3-}$ and (SiO$_4$)$^{4-}$ tetrahedra or for OH groups (c).

shift and morphology of the P-O stretching band within the Raman spectrum; this band is particularly sensitive to the presence of oxygen vacancies [23].

The current study suggests that biochemical reactions exclusive to the Si$_3$N$_4$ surface provided silicic acid (H$_4$SiO$_4$) and ammonia (NH$_3$), both of which were active in regulating cellular metabolism. Evidence is provided that Si from silicic acid and N from ammonia participated in the formation of bony tissue. Similar to prior reports for *in vitro* experiments, these chemical species affected the morphogenetic activity of the osteoblasts by expressing osteoprotegerin (OPG) and the bone morphogenetic protein 2 (BMP2) [28]. While strongly stimulating osteoblast differentiation, they also inhibited formation of osteoclasts (Fig. 12(b)) [28]. This interpretation is also based on previous sRANKL and IGF-1 assessments of the same Si$_3$N$_4$ material *in vitro* [9–12]. Note, however, that, unlike *in vitro* tests, *in vivo* also other types of cell could have interacted with the material and contributed to the observed chemical processes. Pending the clarification of these interesting biological aspects, it remains clear that the availability in bony apatite formation of (SiO$_4$)$^{4-}$ tetrahedra and N anions provides a favorable chemical interface for osteoblastic activity, including a variety of surface charges which enhances protein folding [29], cell motility and proliferation [30,31], and cell signaling by osteocytes [32], (Fig. 12(c)). The ensemble of these factors provides rapid and efficient bone ingrowth for Si$_3$N$_4$ implants. According to the XPS analyses, the average chemical structure of the bony apatite was determined to be Ca$_{10}$(PO(N)$_4$)$_{6-x}$(SiO(N)$_4$)$_x$(OH(N))$_2$□$_x$; where $0 < x < 1$, □ is the OH vacancy, and the N in brackets represents traces of substitutional nitrogen. Pending the availability of additional retrievals, more quantitative analyses will be performed in the future using additional analytical techniques.

Finally, it should be noted that, in specific cases, using biodegradable implants could be the best choice because every small negative effect that a synthetic material could have will eventually fade away while leaving in the human body only osteogenic matter. The problem with biodegradable materials is how to ensure suitable mechanical properties, especially while the synthetic material diminishes in volume. For example, bioglasses

represent the best choice in terms of osteointegration and biocompatibility, but they hardly match strength and reliability issues. It is thus necessary to combine bioactivity and mechanical strength within the same material or with an appropriate design that merges the use of both types of material. In this context, Si$_3$N$_4$ represents a unique choice, which merges some of the advantages of bioglasses and structurally reliable (but bioinert) biomaterials such as PEEK.

## 5. Conclusion

The purpose of this retrieval study was to provide evidence for the unique behavior of Si$_3$N$_4$ in bone tissue engineering. Two short-term intervertebral spinal spacers with comparable *in vivo* service were retrieved and evaluated – a Si$_3$N$_4$ cervical implant and a PEEK lumbar device. The amount of bone growth within the Si$_3$N$_4$ implant was found to be orders of magnitude greater than in the PEEK implant. Obviously, given the difference in vertebral location and the lack of a statistically meaningful number of explants, the present data are not statistical relevant, and should only be considered as case studies for the respective implants. However (and more importantly), the set of independent spectroscopic analyses, including Raman, XPS and FT-IR, consistently demonstrated an important "chemical fingerprint" for the bone grown by human osteoblasts in the neighborhood of the Si$_3$N$_4$ bioceramic's surface. This fingerprint included a modified form of bony apatite in which (SiO$_4$)$^{4-}$ tetrahedra and N anions substituted for (PO$_4$)$^{3-}$ tetrahedra and OH$^-$, respectively. The substituted fractions were not negligible, especially the tetrahedra. According to criteria established within prior *in vitro* experiments using both osteosarcoma and mesenchymal cells, the results of this study fully support the enhanced osteogenesis found for the Si$_3$N$_4$ implant. The availability of Si and N at the surface of Si$_3$N$_4$ is an intriguing aspect of its surface chemistry. The minute release of these elements from the ceramic surface and their favorable biological interaction upregulates the metabolic activity of osteoblasts, which in turn results in rapid and efficient bone growth. In summary, the present data

suggest that in contrast to traditional bioinert compounds (*i.e.*, PEEK), solid $Si_3N_4$ stimulates human cells to produce a "chemically modified" bony apatite, and provides local healing at least comparable to synthetic hydroxyapatite and anti-resorptive drugs.

## Author contribution

Giuseppe Pezzotti conceived the logic of the paper and wrote the manuscript, Naoki Oba performed XPS analyses on the samples, Wenliang Zhu performed the theoretical treatment of XPS spectra leading to their deconvolution and provided the interpretation of the deconvoluted sub-bands, Elia Marin performed Raman spectroscopy experiments, Alfredo Rondinella performed the theoretical treatment of Raman spectra leading to their deconvolution and provided the interpretation of the deconvoluted sub-bands, Francesco Boschetto performed FTIR spectroscopy experiments and performed the theoretical treatment of FTIR spectra leading to their deconvolution and provided the interpretation of the deconvoluted sub-bands, Bryan McEntire provided samples and contributed to the preparation of the manuscript, Kengo Yamamoto conceived and supervised the biological part of this study, and B. Sonny Bal realized the importance of the findings in the medical field, and contributed to the preparation of the manuscript

## Additional information – Financial interests

## References

[1] N. Patel, S.M. Best, W. Bonfield, I.R. Gibson, K.A. Hing, E. Damien, P.A. Revell, A comparative study on the in vivo behavior of hydroxyapatite and silicon substituted hydroxyapatite granules, J. Mater. Sci. Mater. Med. 13 (12) (2002) 1199–1206.

[2] E.-J. Kim, S.-Y. Bu, M.-K. Sung, M.-K. Choi, Effects of silicon on osteoblast activity and bone mineralization of MC3T3-E1 cells, Biol. Trace Elem. Res. 152 (1) (2013) 105–112.

[3] P. Ducheyne, Q. Qiu, Bioactive ceramics: the effect of surface reactivity on bone formation and bone cell function, Biomaterials 20 (1999) 2287–2303.

[4] P. Ducheyne, Bioceramics: material characteristics versus in vivo behavior, J. Biomed. Mater. Res. 21 (A2 Suppl) (1987) 219–236.

[5] K. Wang, C. Zhou, Y. Hong, X. Zhang, A review of protein adsorption on bioceramics, Interface Focus 2 (3) (2012) 259–277.

[6] A.J. Salinas, P. Esbrit, M. Vallet-Regi, A tissue engineering approach based on the use of bioceramics for bone repair, Biomater. Sci. 1 (1) (2013) 40–51.

[7] M. Niinomi, M. Nakai, Titanium-based biomaterials for preventing stress shielding between implant devices and bone, Int. J. Biomater. 2011 (2011) 836587.

[8] R.F.M.R. Kersten, S.M. van Gaalen, M.P. Arts, K.C.B. Roes, A. de Gast, T.P. Corbin, F.C. Öner, The SNAP trial: a double blind multi-center randomized controlled trial of a silicon nitride versus a PEEK cage in transforaminal lumbar interbody fusion in patients with symptomatic degenerative lumbar disc disorders: study protocol, BMC Musculoskel. Disord. 57 (2014) 15.

[9] G. Pezzotti, B.J. McEntire, R.M. Bock, W. Zhu, F. Boschetto, A. Rondinella, E. Marin, Y. Marunaka, T. Adachi, T. Yamamoto, N. Kanamura, B.S. Bal, In situ spectroscopic screening of osteosarcoma living cells on stoichiometry-modulated silicon nitride bioceramic surfaces, ACS Biomater. Sci. Eng. 2 (7) (2016) 1121–1134.

[10] G. Pezzotti, B.J. McEntire, R. Bock, M. Boffelli, W. Zhu, E. Vitale, L. Puppulin, T. Adachi, T. Yamamoto, N. Kanamura, B.S. Bal, Silicon nitride: a synthetic mineral for vertebrate biology, Sci. Rep. 6 (2016) 31717.

[11] G. Pezzotti, E. Marin, T. Adachi, A. Rondinella, F. Boschetto, W.-L. Zhu, N. Sugano, R.M. Bock, B.J. McEntire, B.S. Bal, Bioactive silicon nitride: a new therapeutic material for osteoarthropathy, Sci. Rep. 7 (2017) 44848.

[12] G. Pezzotti, R.M. Bock, T. Adachi, A. Rondinella, F. Boschetto, W. Zhu, E. Marin, B.J. McEntire, B.J. McEntire, B.S. Bal, O. Mazda, Silicon nitride surface chemistry: a potent regulator of mesenchymal cell activity for bone formation, Appl. Mater. Today 9 (2017) 82–95.

[13] D.M. Reffitt, N. Ogston, R. Jugdaohsingh, H.F.J. Cheung, B.A.J. Evans, R.P.H. Thompson, J.J. Powell, G.N. Hampson, Orthosilicic acid stimulates collagen type 1 synthesis and osteoblastic differentiation in human osteoblast-like cells in vitro, Bone 32 (2) (2003) 127–135.

[14] J.R. Henstock, L.T. Canham, S.I. Anderson, Silicon: the evolution of its use in biomaterials, Acta Biomater. 11 (2015) 17–26.

[15] M.-Y. Shie, S.-J. Ding, H.-C. Chang, The role of silicon in osteoblast-like cell proliferation and apoptosis, Acta Biomater. 7 (6) (2011) 2604–2614.

[16] E.S. Thian, J. Huang, S.M. Best, Z.H. Barber, R.A. Brooks, N. Rushton, W. Bonfield, The response of osteoblasts to nanocrystalline silicon-substituted hydroxyapatite thin films, Biomaterials 27 (13) (2006) 2692–2698.

[17] A. Ilyas, T. Odatsu, A. Shah, F. Monte, H.K.W. Kim, P. Kramer, P.B. Aswath, V.G. Varanasi, Amorphous silica: a new antioxidant role for rapid critcal-sized bone defect healing, Adv. Healthc. Mater. 6 (2016) 1–12.

[18] T.J. Webster, A.A. Patel, M.N. Rahaman, B.S. Bal, Anti-infective and osteointegration properties of silicon nitride, poly (ether ether ketone), and titanium implants, Acta Biomater. 8 (12) (2012) 4447–4454.

[19] S.K. Sinclair, G.J. Konz, J.M. Dawson, R.T. Epperson, R.D. Bloebaum, Host bone response to polyetheretherketone versus porous tantalum implants for cervical spinal fusion in a goat model, Spine (Phila. Pa. 1976) 37 (10) (2012).

[20] G. Singh, S. Singh, S. Prakash, surface characterization of plasma sprayed pure and reinforced hydroxyapatite coating on Ti6Al4V alloy, Surf. Coat. Technol. 205 (20) (2011) 4814–4820.

[21] M.M. Figueiredo, A.G. Martins, J.A.F. Gamelas, Characterization of Bone and Bone-Based Graft Materials using FTIR Spectroscopy, INTECH Open Access, Rijeka, Croatia, 2012, pp. 315–338.

[22] K. Nakata, T. Kubo, C. Numako, T. Onoki, A. Nakahira, Synthesis and characterization of silicon-doped hydroxyapatite, Mater. Trans. 50 (5) (2009) 1046–1049.

[23] D. Marchat, M. Zymelka, C. Coelho, L. Gremillard, L. Joly-pottuz, F. Babonneau, C. Esnouf, J. Chevalier, D. Bernache-Assollant, Accurate characterization of pure silicon-substituted hydroxyapatite powders synthesized by a new precipitation route, Acta Biomater. 9 (6) (2013) 6992–7004.

[24] I. Kansal, A. Goel, D.U. Tulyaganov, L.F. Santos, J.M.F. Ferreira, Structure, surface reactivity and physico-chemical degradation of fluoride containing phospho-silicate glasses, J. Mater. Chem. 21 (22) (2011) 8074–8084.

[25] A. Boskey, N. Pleshko Camacho, FT-IR imaging of native and tissue-engineered bone and cartilage, Biomaterials 28 (15) (2007) 2465–2478.

[26] G. Ulian, G. Valdrè, M. Corno, P. Ugliengo, The vibrational features of hydroxylapatite and type A carbonated apatite: a first principle contribution, Am. Mineral. 98 (4) (2013) 752–759.

[27] S. Zou, J. Huang, S. Best, W. Bonfield, Crystal imperfection studies of pure and silicon substituted hydroxyapatite using raman and XRD, J. Mater. Sci. Mater. Med. 16 (12) (2005) 1143–1148.

[28] G.R. Beck, S.-W.W. Ha, C.E. Camalier, M. Yamaguchi, Y. Li, J.-K.K. Lee, M.N. Weitzmann, Bioactive silica-based nanoparticles stimulate bone-forming osteoblasts, suppress bone-resorbing osteoclasts, and enhance bone mineral density in vivo, Nanomed. Nanotechnol. Biol. Med. 8 (6) (2012) 793–803.

[29] L.A. Capriotti, T.P. Beebe, J.P. Schneider, Hydroxyapatite surface-induced peptide folding, J. Am. Chem. Soc. 129 (16) (2007) 5281–5287.

[30] B. Feng, J. Weng, B.C. Yang, S.X. Qu, D. Zhang X, Characterization of titanium surfaces with calcium and phosphate and osteoblast adhesion, Biomaterials 25 (17) (2004) 3421–3428.

[31] T.R. Rautray, R. Narayanan, K.-H. Kim, Ion implantation of titanium based biomaterials, Prog. Mater. Sci. 56 (8) (2011) 1137–1177.

[32] B.D. Boyan, S. Lossdorfer, L. Wang, G. Zhao, C.H. Lohmann, D.L. Cochran, Z. Schwartz, Osteoblasts generate an osteogenic microenvironment when grown on surfaces with rough microtopographies, Eur. Cells Mater. 5 (2) (2003) 11–12.